

# Investigation on Unbalanced Mach–Zehnder Interferometer

Mao-Feng Tseng, mike13112@gmail.com

## I. INTRODUCTION

THE Mach–Zehnder Interferometer (MZI) is to demonstrate optical interference by dividing a light beam into two paths using a beamsplitter and then recombining them with a second beamsplitter. The output intensity depends on the relative phase difference between the two paths, enabling precise control of the interference pattern. Due to its sensitivity to phase changes, the MZI serves as the foundation for various optical modulators—such as electro-optic and thermo-optic modulators—used in integrated photonics and optoelectronics. In this report, we propose a Mach–Zehnder Interferometer design and present its simulation results.

## II. THEORY

First, consider a Y-branch splitter. We start with an input light of intensity  $I_i$  and electric field  $E_i$ . The splitter divides the light equally into two branches, resulting in output intensities  $I_1 = I_2 = I_i/2$  and electric fields  $E_1 = E_2 = E_i/\sqrt{2}$ . At the combiner, the light entering one branch is also split—part couples into the fundamental mode of the output waveguide, while the remainder couples into higher-order or radiation modes. As the result, the electric field at the combiner port is  $E_{o1} = E_1/\sqrt{2}$  or  $E_{o2} = E_2/\sqrt{2}$ . The output field is given by the vector sum of the input fields divided by a factor of  $\sqrt{2}$ , which in turn  $E_o = (E_1 + E_2)/\sqrt{2}$ . For a plane wave, the electric field is given by  $E = E_0 e^{i(\omega t - \beta z)}$ , where the propagation constant  $\beta = \frac{2\pi n}{\lambda}$ , with  $n$  being the refractive index and  $\lambda$  the wavelength. If it is lossless, the output electric fields from the two channels of the Y-branch are given by:

$$E_{o1} = E_1 e^{-i\beta L_1} = \frac{E_i}{\sqrt{2}} e^{-i\beta L_1}$$

$$E_{o2} = E_2 e^{-i\beta L_2} = \frac{E_i}{\sqrt{2}} e^{-i\beta L_2}$$

The total output field after recombination is the sum of these two fields:

$$E_o = \frac{1}{\sqrt{2}} E_{o1} + \frac{1}{\sqrt{2}} E_{o2} = E_i \left( \frac{e^{-i\beta L_1} + e^{-i\beta L_2}}{2} \right)$$

The corresponding output intensity is:

$$I_o = |E_o|^2 = \frac{I_i}{4} |e^{-i\beta L_1} + e^{-i\beta L_2}|^2 = \frac{I_i}{2} [1 + \cos(\beta\Delta L)]$$

where  $\Delta L = L_2 - L_1$  is the path length difference between the two channels. The transfer function of the Mach–Zehnder Interferometer (MZI) can be expressed as:

$$T_{\text{MZI}}(\lambda) = \frac{1}{2} [1 + \cos(\beta\Delta L)]$$

In this report, we designed and fabricated unbalanced MZIs with different  $\Delta L$ : 50um, 100um, 150um, 250um and 400um as shown in Figure1. The width and height of the strip waveguide in this device are 500nm and 220nm, respectively. The fabricated MZIs were measured and compared with simulated results from Lumerical INTERCONNECT.

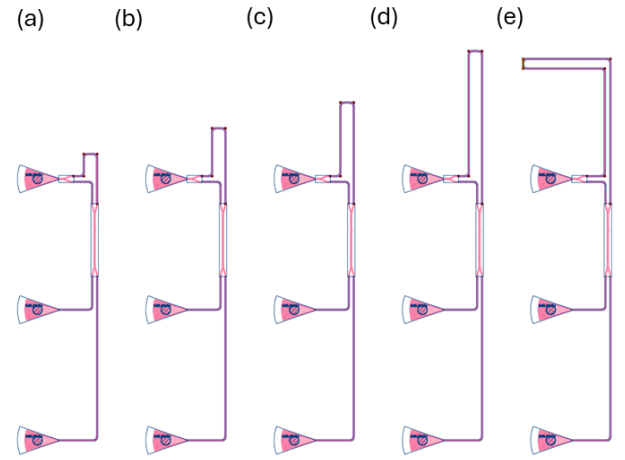


Figure1. Design layout of unbalanced MZI with  $\Delta L$  of (a)50um, (b)100um, (c)150um, (d)250um and (e)400um.

## III. MODELLING AND SIMULATION

### A. Waveguide

In our design, we first simulated the strip waveguides with widths of 400 nm, 500 nm, 600 nm, and 700 nm, with a fixed height of 220 nm. Figure 2 illustrates the electric field intensity distribution for the transverse electric (TE) mode and the corresponding distribution for the transverse magnetic (TM) mode.

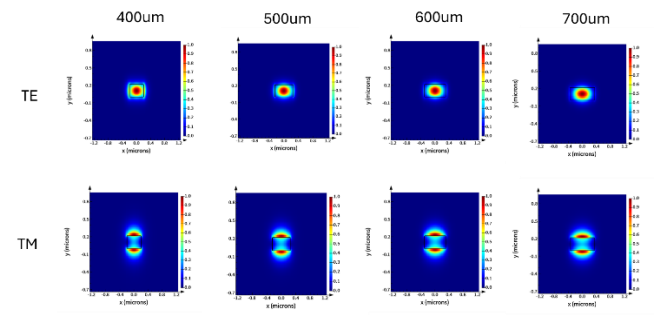


Figure2. Electric field intensity of TE and TM mode in the waveguide.

For waveguide with 400 nm width, a significant portion of the optical field extends into the cladding as an evanescent wave. Conversely, as the width increases to 700 nm, the TE mode becomes tightly confined within the silicon core. In contrast, the TM mode profiles remain relatively stable across all widths. This behavior is attributed to the fixed waveguide height of 220 nm, which serves as the primary geometric constraint for the vertically polarized TM mode.

Figures 3 and 4 show the variation of the effective refractive index and group index( $n_g$ ) as functions of wavelength in TE mode in the waveguide with various width, respectively. We observed a consistent increase in the real part of  $n_{eff}$  as the width expanded, rising from approximately 2.24 at 400nm width to 2.64 at 700 nm width(at  $\lambda = 1550\text{nm}$ ). Furthermore, the negligible imaginary part of the effective index ( $k_{eff} \sim 10^{-9}$ ) indicates that propagation losses due to material absorption are minimal in the simulation for this design.

The 400nm waveguide exhibits the highest group index ( $n_g \sim 4.4$  at  $\lambda = 1550\text{nm}$ ). As the width increases,  $n_g$  decreases, stabilizing around 3.97 for the 700 nm width. Notably, the slope of the group index versus wavelength, representing the group velocity dispersion undergoes a sign inversion between 400 nm and 500 nm.

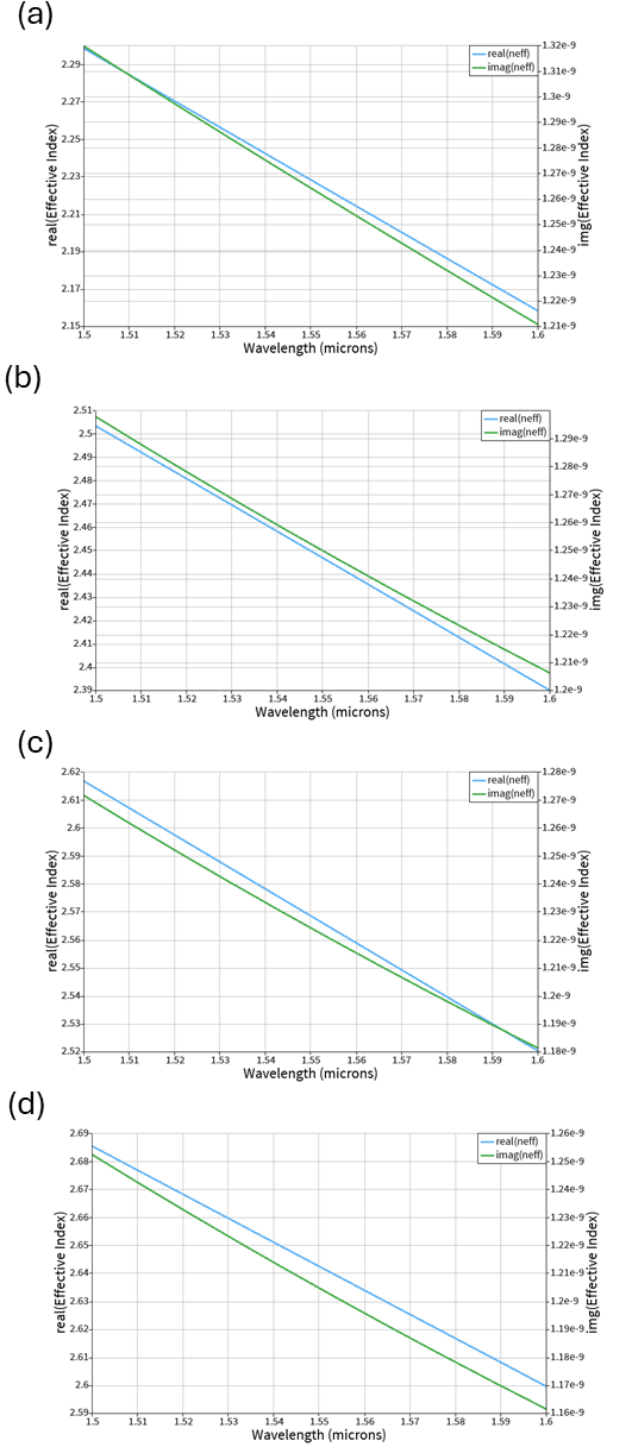


Figure 3. Effective index of the waveguide vs. wavelength with width of (a) 400nm, (b) 500nm, (c) 600nm, (d) 700nm.

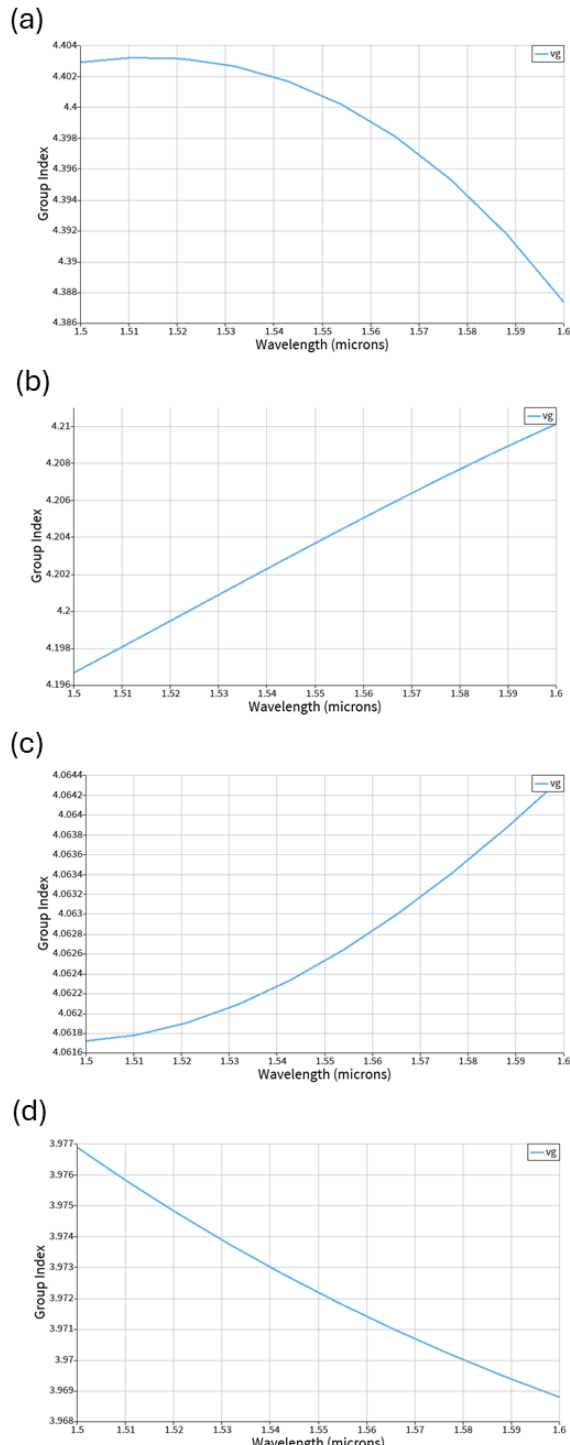


Figure 4. Group index of the waveguide vs. wavelength with width of (a) 400nm, (b) 500nm, (c) 600nm, (d) 700nm.

A compact model for the wavelength-dependent effective index was derived as:

$$n_{\text{eff}}(\lambda) = n_1 + n_2(\lambda - \lambda_0) + n_3(\lambda - \lambda_0)^2$$

where  $\lambda_0$  is the reference wavelength. Based on the effective index from the simulation results, we can obtain  $n_1$ ,  $n_2$  and  $n_3$  of the compact model by curve fitting in MATLAB. The results are listed in Table I. As expected based on the modal analysis,  $n_1$  increases monotonically from 2.2283 to 2.6425 as the width expands from 400 nm to 700 nm. The negative values of the first-order coefficient  $n_2$  across all widths indicate that the effective index decreases with increasing wavelength. The magnitude of  $n_2$  decreases (becomes less negative) as the width increases (from -1.4008 at 400 nm to -0.8580 at 700 nm). A notable sign inversion of the second-order coefficient  $n_3$  is observed, it transitions from positive (0.0476) at 400 nm to negative values at 500 nm and 600 nm, before reverting to positive at 700 nm. This mathematical inversion aligns with the slope changes observed in the group index plots (Figure 3) discussed earlier. In this report, 500nm width is selected for the fabrication of the MZIs in the design.

Waveguide width	$n_1$	$n_2$	$n_3$
400nm	2.2283	-1.4008	0.0476
500nm	2.4468	-1.1334	-0.0439
600nm	2.5686	-0.9639	-0.0088
700nm	2.6425	-0.8580	0.0260

Table I.  $n_1$ ,  $n_2$  and  $n_3$  fitted with compact model at different waveguide width.

#### B. Mach-Zehnder Interferometer

We compared the measurement results and simulation from Lumerial INTERCONNECT, which is shown in Figure 5. A spectral offset is observed between measurement results and simulation. This can be caused by deviations in the effective index  $n_{\text{eff}}$ . A variation in waveguide width of just 1–2 nm during fabrication can significantly change  $n_{\text{eff}}$ , shifting the interference peaks. To accurately extract the free spectral range(FSR), baseline correction and curve fitting were applied to the measurement data as shown in Figure 6.

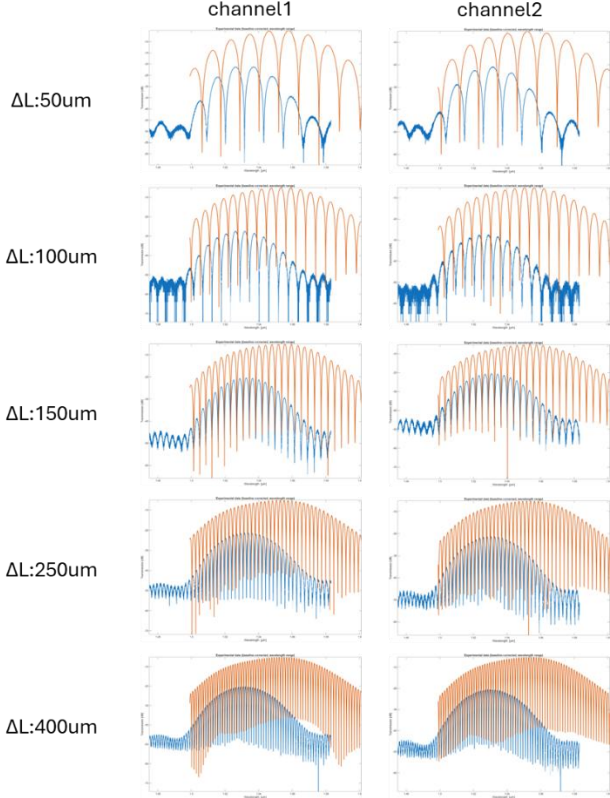


Figure 5. Comparison of measurement results(blue) and simulation from Lumerical INTERCONNECT(orange).

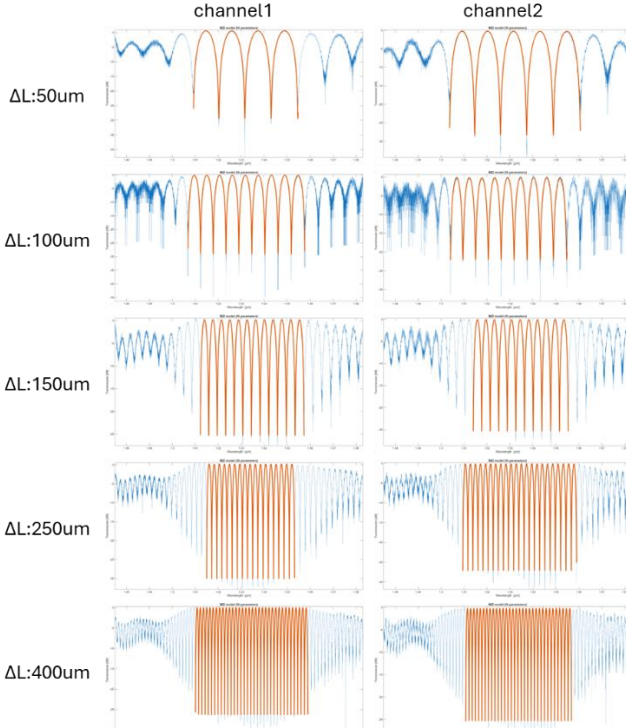


Figure 6. Comparison of measurement results(blue) and simulation from Lumerical INTERCONNECT(orange).

The interference peaks in each channel are identified to define FSR. The FSR of the peaks closest to 1550nm is summarized in Table II. Except the MZI with  $\Delta L: 100\mu m$ , measurement data shows minimal deviation from simulation, which suggests the deviation in MZI with  $\Delta L: 100\mu m$  may come from the control limitation in fabrication.

$\Delta L(\mu m)$	channel1 FSR		channel2 FSR	
	measure	simulation	measure	simulation
50	11.68	11.68	11.95	11.77
100	5.70	5.80	5.60	5.80
150	3.81	3.86	3.84	3.86
250	2.30	2.31	2.30	2.31
400	1.46	1.46	1.46	1.46

Table II. FSR identified by peaks with different  $\Delta L$ .

Since FSR is given by:

$$FSR = \frac{\lambda^2}{n_g \Delta L}$$

where  $n_g$  is the group index and  $\Delta L$  is the path length difference between the two arms. Therefore, we can calculate  $n_g$  from FSR with curve-fitted MZI transfer function. The calculated  $n_g$  for various  $\Delta L$  values used in our design is summarized in Table III. Theoretically,  $n_g$  is a property of the waveguide cross-section and should be constant regardless of the MZI length. The fact that  $n_g$  drops slightly for the longest path length difference device ( $\Delta L = 400\mu m$ ) suggests that the fabrication quality (width uniformity) might vary across the devices. The extracted  $n_g$  values consistently locate around 4.08 to 4.17, validating the waveguide design geometry. The minor fluctuations across different devices suggest slight spatial non-uniformity in fabrication across the wafer. A higher deviation is observed for the MZI with shorter  $\Delta L$ . This may be attributed to the bending effect, which is more significant with shorter waveguide.

$\Delta L(\mu\text{m})$	channel	ng	
		measure	simulation
50	1	4.1193	4.1002
	2	4.0942	4.0990
100	1	4.1416	4.1457
	2	4.1562	4.1450
150	1	4.1684	4.1609
	2	4.1684	4.1609
250	1	4.1684	4.1730
	2	4.1773	4.1726
400	1	4.0874	4.0840
	2	4.0881	4.0838

Table III. ng calculated from measurement and simulation with different  $\Delta L$ .

#### IV. CONCLUSION

In this report, we designed and investigated unbalanced MZIs with various path length differences  $\Delta L$ . We simulated strip waveguides with different widths, selecting 500 nm for fabrication. While a spectral shift due to fabrication tolerances was observed, the calculated FSR and  $n_g$  show strong agreement with simulation, particularly for devices with longer path length differences where bend-induced errors are minimized.

#### APPENDIX

##### A. Fabrication description

Fabricated is performed at one or more of these: Applied Nanotools and Washington Nanofabrication Facility. The following are the process descriptions.

##### Applied Nanotools, Inc. NanoSOI process:

The photonic devices were fabricated using the NanoSOI MPW fabrication process by Applied Nanotools Inc. (<http://www.appliednt.com/nanosoi>; Edmonton, Canada) which is based on direct-write 100 keV electron beam lithography technology. Silicon-on-insulator wafers of 200 mm diameter, 220 nm device thickness and 2  $\mu\text{m}$  buffer oxide thickness are used as the base material for the fabrication. The wafer was pre-diced into square substrates with dimensions of 25x25 mm, and lines were scribed into the substrate backsides to facilitate easy separation into smaller chips once fabrication was complete. After an initial wafer clean using piranha solution (3:1 H<sub>2</sub>SO<sub>4</sub>:H<sub>2</sub>O<sub>2</sub>) for 15 minutes and water/IPA rinse, hydrogen silsesquioxane (HSQ) resist was spin-coated onto the substrate and heated to evaporate the solvent. The photonic devices were patterned using a JEOL JBX-8100FS electron beam instrument at The University of British

Columbia. The exposure dosage of the design was corrected for proximity effects that result from the backscatter of electrons from exposure of nearby features. Shape writing order was optimized for efficient patterning and minimal beam drift. After the e-beam exposure and subsequent development with a tetramethylammonium sulfate (TMAH) solution, the devices were inspected optically for residues and/or defects. The chips were then mounted on a 4" handle wafer and underwent an anisotropic ICP-RIE etch process using chlorine after qualification of the etch rate. The resist was removed from the surface of the devices using a 10:1 buffer oxide wet etch, and the devices were inspected using a scanning electron microscope (SEM) to verify patterning and etch quality. A 2.2  $\mu\text{m}$  oxide cladding was deposited using a plasma-enhanced chemical vapour deposition (PECVD) process based on tetraethyl orthosilicate (TEOS) at 300°C. Reflectometry measurements were performed throughout the process to verify the device layer, buffer oxide and cladding thicknesses before delivery.

##### Washington Nanofabrication Facility (WNF) silicon photonics process

The devices were fabricated using 100 keV Electron Beam Lithography [1]. The fabrication used silicon-on-insulator wafer with 220 nm thick silicon on 3  $\mu\text{m}$  thick silicon dioxide. The substrates were 25 mm squares diced from 150 mm wafers. After a solvent rinse and hot-plate dehydration bake, hydrogen silsesquioxane resist (HSQ, Dow-Corning XP-1541-006) was spin-coated at 4000 rpm, then hotplate baked at 80 °C for 4 minutes. Electron beam lithography was performed using a JEOL JBX-6300FS system operated at 100 keV energy, 8 nA beam current, and 500  $\mu\text{m}$  exposure field size. The machine grid used for shape placement was 1 nm, while the beam stepping grid, the spacing between dwell points during the shape writing, was 6 nm. An exposure dose of 2800  $\mu\text{C}/\text{cm}^2$  was used. The resist was developed by immersion in 25% tetramethylammonium hydroxide for 4 minutes, followed by a flowing deionized water rinse for 60 s, an isopropanol rinse for 10 s, and then blown dry with nitrogen. The silicon was removed from unexposed areas using inductively coupled plasma etching in an Oxford Plasmalab System 100, with a chlorine gas flow of 20 sccm, pressure of 12 mT, ICP power of 800 W, bias power of 40 W, and a platen temperature of 20 °C, resulting in a bias voltage of 185 V. During etching, chips were mounted on a 100 mm silicon carrier wafer using perfluoropolyether vacuum oil. Cladding oxide was deposited using plasma enhanced chemical vapor deposition (PECVD) in an Oxford Plasmalab System 100 with a silane (SiH<sub>4</sub>) flow of 13.0 sccm, nitrous oxide (N<sub>2</sub>O) flow of 1000.0 sccm, high-purity nitrogen (N<sub>2</sub>) flow of 500.0 sccm, pressure at 1400mT, high-frequency RF power of 120W, and a platen temperature of 350C. During deposition, chips rest directly on a silicon carrier wafer and are buffered by silicon pieces on all sides to aid uniformity.

### B. Measurement description

To characterize the devices, a custom-built automated test setup [2, 6] with automated control software written in Python was used [3]. An Agilent 81600B tunable laser was used as the input source and Agilent 81635A optical power sensors as the output detectors. The wavelength was swept from 1500 to 1600 nm in 10 pm steps. A polarization maintaining (PM) fibre was used to maintain the polarization state of the light, to couple the TE polarization into the grating couplers [4]. A 90° rotation was used to inject light into the TM grating couplers [4]. A polarization maintaining fibre array was used to couple light in/out of the chip [5].

### ACKNOWLEDGMENT

I/We acknowledge the edX UBCx Phot1x Silicon Photonics Design, Fabrication and Data Analysis course, which is supported by the Natural Sciences and Engineering Research Council of Canada (NSERC) Silicon Electronic-Photonic Integrated Circuits (SiEPIC) Program. The devices were fabricated by Richard Bojko at the University of Washington Washington Nanofabrication Facility, part of the National Science Foundation's National Nanotechnology Infrastructure Network (NNIN), and Cameron Horvath at Applied Nanotools, Inc. Omid Esmaeeli performed the measurements at The University of British Columbia. We acknowledge Lumerical Solutions, Inc., Mathworks, Mentor Graphics, Python, and KLayout for the design software.

### REFERENCES

- [1] R. J. Bojko, J. Li, L. He, T. Baehr-Jones, M. Hochberg, and Y. Aida, "Electron beam lithography writing strategies for low loss, high confinement silicon optical waveguides," *J. Vacuum Sci. Technol. B* 29, 06F309 (2011)
- [2] Lukas Chrostowski, Michael Hochberg, chapter 12 in "Silicon Photonics Design: From Devices to Systems", Cambridge University Press, 2015
- [3] <http://siepic.ubc.ca/probestation>, using Python code developed by Michael Caverley
- [4] Yun Wang, Xu Wang, Jonas Flueckiger, Han Yun, Wei Shi, Richard Bojko, Nicolas A. F. Jaeger, Lukas Chrostowski, "Focusing sub-wavelength grating couplers with low back reflections for rapid prototyping of silicon photonic circuits", *Optics Express* Vol. 22, Issue 17, pp. 20652-20662 (2014) doi: 10.1364/OE.22.020652
- [5] [www.picconnections.com](http://www.picconnections.com), PLC Connections, Columbus OH, USA.
- [6] <http://mapleleafphotonics.com>, Maple Leaf Photonics, Seattle WA, USA.